Land-ocean differences in tropical deep convective clouds: intercomparison of DYAMOND simulations and CloudSat observations

Takahashi, H. ORCID: https://orcid.org/0000-0002-0578-8605, Wu, L. ORCID: https://orcid.org/0000-0001-8447-8180, Smalley, M. A. ORCID: https://orcid.org/0000-0002-0731-6759, Stephens, G. ORCID: https://orcid.org/0000-0002-9860-0287, Suzuki, K. ORCID: https://orcid.org/0000-0001-5315-2452 and Posselt, D. J. (2025) Land-ocean differences in tropical deep convective clouds: intercomparison of DYAMOND simulations and CloudSat observations. Journal of Geophysical Research: Atmospheres, 130 (23). e2025JD044688. ISSN 2169-8996 doi: 10.1029/2025jd044688 Available at https://centaur.reading.ac.uk/127676/

JGR Atmospheres

RESEARCH ARTICLE
10.1029/2025JD044688

Land-Ocean Differences in Tropical Deep Convective Clouds: Intercomparison of DYAMOND Simulations and CloudSat Observations

Hanii Takahashi[1], Longtao Wu[1], Mark A. Smalley[1,2], Graeme Stephens[1,3], Kentaroh Suzuki[4], and Derek J. Posselt[1]

[1]Jet Propulsion Laboratory, California Institute of Technology, Pasadena, CA, USA, [2]Joint Institute for Regional Earth System Science and Engineering, University of California, Los Angeles, CA, USA, [3]Department of Meteorology, University of Reading, Reading, UK, [4]Atmosphere and Ocean Research Institute, The University of Tokyo, Chiba, Japan

Key Points:

- CloudSat observations evaluate land-ocean differences in deep convection and environments represented in DYnamics of the Atmospheric general circulation Modeled On Non-hydrostatic Domains simulations
- Simulations overestimate convection intensity in the Tropical Warm Pool due to unrealistic energy conversion efficiency
- Precipitation forms at high altitudes with weak updrafts, indicating issues in modeling cloud dynamics and microphysics

Supporting Information:

Supporting Information may be found in the online version of this article.

Correspondence to:

H. Takahashi,
Hanii.Takahashi@jpl.nasa.gov

Citation:

Takahashi, H., Wu, L., Smalley, M. A., Stephens, G., Suzuki, K., & Posselt, D. J. (2025). Land-ocean differences in tropical deep convective clouds: Intercomparison of DYAMOND simulations and CloudSat observations. *Journal of Geophysical Research: Atmospheres*, *130*, e2025JD044688. https://doi.org/10.1029/2025JD044688

Received 24 JUN 2025
Accepted 31 OCT 2025

Abstract This study investigates how deep convective clouds and their surrounding environments are represented in the DYnamics of the Atmospheric general circulation Modeled On Non-hydrostatic Domains (DYAMOND) simulations by comparing them with CloudSat observations across three tropical "chimney zones": Tropical Africa, Tropical Amazonia, and the Tropical Warm Pool (TWP). These regions, spanning a spectrum of land-ocean contrasts, exhibit distinct environmental and convective characteristics. While DYAMOND simulations capture environmental differences among the regions, biases persist in representing convective intensity and precipitation dynamics. The simulations overestimate convective intensity in the TWP, likely due to higher-than-realistic conversion efficiencies of potential energy to kinetic energy. Precipitation formation also deviates from observations, occurring at higher altitudes with weak vertical velocities, indicating misrepresentations in cloud microphysics and updraft dynamics. These findings highlight the need for improved coupling of cloud dynamics and microphysics in global models to better simulate deep convection and its environmental interactions.

Plain Language Summary This study investigates how well DYnamics of the Atmospheric general circulation Modeled On Non-hydrostatic Domains (DYAMOND) computer simulations represent deep convective clouds and their environments by comparing them with satellite observations from CloudSat. We focus on three tropical regions known for thunderstorms: Tropical Africa, Tropical Amazonia, and the Tropical Warm Pool (TWP). These regions represent a mix of land and ocean environments, each with unique weather patterns. While the DYAMOND simulations perform well in capturing differences in the environments between these regions, they face challenges in accurately modeling the strength of convection and how precipitation forms. For example, the simulations overestimate storm intensity in the TWP, probably because they unrealistically convert too much potential energy into storm motion. They also show rain forming too high up in the atmosphere with weak upward winds, which suggests issues with how the models handle cloud processes. These findings suggest the need to improve how these models connect cloud dynamics and precipitation processes.

1. Introduction

Convective processes are key in the dynamics of the tropical atmosphere. Among the myriad processes active within deep convection, the vertical mass transport facilitated by convective updraft cores, plays a crucial role in dictating the tropical energy budgets and hydrological cycles (Riehl & Malkus, 1958). A significant process influencing vertical transport is entrainment, which dilutes the strength of convective updraft cores and thereby weakens the intensity of vertical transport (Houze, 2014). However, a detailed exploration of these fundamental convective processes, especially their differences across land and ocean, has only recently become possible through systematic global satellite observations. This gap has existed because no previous or current satellite instruments were able to directly measure updraft velocity, convective mass flux, or quantify entrainment/detrainment, posing challenges in accurately simulating deep convective clouds and realistically delineating contrasts between continental and oceanic deep convection within weather and climate models. The recently launched EarthCARE mission (Illingworth et al., 2015; Wehr et al., 2023) and upcoming INvestigation of Convective Updrafts (INCUS; van den Heever, 2021) mission, aim to address these limitations with its advanced observational capabilities. While EarthCARE and INCUS will greatly expand our knowledge of deep convective

physical processes, we can already gain valuable insights from the observations collected by the CloudSat Cloud Profiling Radar (CPR; Stephens et al., 2008).

To address these challenges, a series of publications describe analyses of CloudSat/A-Train multi-sensor observations that are used to explore convective dynamics, structure, and environment (Takahashi et al., 2017, 2021, 2023, 2024; Takahashi & Luo, 2012, 2014). These studies demonstrate a positive correlation between convective strength and core size (e.g., Byers Braham, 1949; LeMone & Zipser, 1980; Riehl & Malkus, 1958), while revealing an inverse correlation between convective core size and entrainment rate (defined as fractional increase in cloud mass per unit height). This latter inverse relationship has been a fundamental assumption in cumulus cloud modeling, influencing the modeling of convective clouds for over 50 years (Simpson & Wiggert, 1969). Takahashi et al. (2021) provided observational evidence supporting this inverse relationship, originally derived from a multi-year CloudSat survey in which entrainment rates were estimated based on convective outflow levels relative to the level of neutral buoyancy calculated from ambient soundings. Subsequent findings from these studies highlight pronounced differences between land and ocean in convective characteristics: deep convective systems over land tend to be smaller overall compared to those over the ocean, yet paradoxically the convective cores over land are larger, stronger, and less affected by entrainment, indicating more intense vertical mass transport by continental convective cores.

So, what causes these land-ocean differences in convective characteristics? The dynamics of convection over land and ocean are fundamentally different. The ocean can absorb the Sun's energy without significant heating through evaporation and by turbulence transport of energy within the ocean's mixed layer away from the surface. By contrast, land heats up quickly, transferring sensible heat to the air above and creating a pronounced increase in near-surface buoyancy. This burst of heat causes columns of warm, buoyant air to ascend more quickly over land than over the ocean, where the surface warms more gradually. Thus, the contrast in convective cloud characteristics between land and ocean can be attributed to the surface's heat capacity, called the thermal hypothesis (Williams & Stanfill, 2002). Building on this framework, the recent study by Takahashi et al. (2023) investigates deeper into the causes behind the land-ocean contrasts in convective cloud characteristics, particularly examining why convective cores are wider and why entrainment dilution is weaker over land based on CloudSat observations. Their findings suggest that by viewing tropical deep convection as a process that transforms potential energy into kinetic energy, the reasons for the intensified convection over land become clear. This enhancement is due to more effective energy conversion, enabled by broader updraft cores that experience less mixing with the surrounding air. The conversion efficiency and the extent of mixing with ambient air are significantly influenced by the lifting condensation level (LCL), which marks the behavior of dry air parcels ascending before cloud formation, underscoring the pivotal role of these parcels' dry stage in laying the groundwork for subsequent deep convection (Mulholland et al., 2021; Takahashi et al., 2023; Williams & Stanfill, 2002).

Through the development of new analysis methodologies based on CloudSat/A-Train multi-sensor observations, this series of publications (Takahashi et al., 2017, 2021, 2023, 2024; Takahashi & Luo, 2012, 2014) has begun to examine the land-ocean differences in the convective properties, structure, and environment of tropical deep convection. These methodologies offer novel diagnostic tools to compare models with observations. In the past, the difficulty confronting the direct comparison with observations arises from the coarse resolution of General Circulation Models (GCMs), which is approximately 100 km (e.g., Gnitou et al., 2023). Although Convection-Resolving Models (CRMs) offer finer resolutions, they are typically confined to regional, not global scales, complicating comprehensive analyses of land-ocean contrasts. The DYnamics of the Atmospheric general circulation Modeled On Non-hydrostatic Domains (DYAMOND; Stevens et al., 2019) initiative supported by the Centre of Excellence in Simulation of Weather and Climate in Europe (CESiWACE) now offers the potential to match observations and diagnostic tools developed for observations like those from CloudSat/A-Train to global simulations with comparable resolutions. DYAMOND simulations employ global models with storm-resolving grids at km-scale resolutions. The success of the initial experiment spurred the launch of DYAMOND Winter, which simulated the period from 20 January to 1 March 2020, and is the focus of this study.

Our goal is to enhance knowledge of convective processes by examining how deep convective clouds and related processes are expressed in models by identifying where models. simulate observations well and where potential biases exist in the context of land-ocean contrasts in deep convection. To this end, we investigate three climatologically distinctive tropical regions that showcase a range of environments, from highly continental to distinctly oceanic: Tropical Africa (5°–40°E, 15°S–15°N), Tropical Amazonia (80°–35°W, 25°S–5°N), and the

Tropical Warm Pool (TWP, 90°–180°E, 15°S–15°N), following the methodology of Takahashi et al. (2023). Tropical Africa, Tropical Amazonia, and TWP are known as the three major tropical "chimney zones" due to their prevalent deep convection (Williams & Stanfill, 2002). Specifically, Tropical Africa is marked by the most continental conditions and the most intense convection (Zipser et al., 2006), Tropical Amazonia features a transitional environment, earning it the label "green ocean" (Wang et al., 2018), and the TWP is the most oceanic, exhibiting the weakest convection among the three (e.g., Liu et al., 2007; Takahashi & Luo, 2014). By contrasting the environmental parameters and convective cloud properties across these regions, we aim to illustrate how effectively DYAMOND simulations capture the contrast between land and ocean and how the dynamics of convective storms are linked to their environments. The rest of the paper is organized as follows: Section 2 describes the data sources and analysis methods, results and interpretations are presented in Section 3, and Section 4 summarizes and discusses our findings.

2. Data

2.1. Satellite Data Description

CloudSat is a sun-synchronous, polar-orbiting satellite equipped with a 94 GHz CPR sensitive to both cloud and precipitation-sized particles. The satellite crosses the equator at approximately 1:30 a.m./p.m local time, achieving horizontal resolutions of 1.7 km along track and 1.3 km across track, with a vertical resolution of 480 m, which is oversampled to 240 m. Similar to previous studies (e.g., Takahashi et al., 2023), we utilize two CloudSat products: 2B-GEOPROF (Marchand & Mace, 2018) and ECMWF-AUX (Cronk & Partain, 2017). The 2B-GEOPROF data includes radar reflectivity and a cloud mask, using a threshold of cloud mask $\geq$20 for moderate-confidence cloud detection, indicating that radar reflectivity measurements are likely due to hydrometeors (Bacmeister & Stephens, 2011; Riley & Mapes, 2009). The ECMWF-AUX data provides vertical temperature and moisture profiles from the European Centre for Medium-Range Weather Forecast (ECMWF) operational forecast, 3-hr and 50-km interpolated in space and time to match the CloudSat track. Comprehensive information on the CloudSat mission is provided by Stephens et al. (2008).

We used CloudSat because its 94-GHz CPR is highly sensitive to both cloud particles and precipitation-sized hydrometeors. Our motivation is to examine land–ocean differences in convective properties, structures, and environments; having full vertical profiles of clouds is therefore essential. This is something that, for example, the Tropical Rainfall Measuring Mission (TRMM; Kummerow, 1998; Kummerow et al., 1998; Liu et al., 2012), which primarily focuses on precipitation, cannot fully capture. Moreover, since our goal is to investigate how the dynamics of convective storms are linked to their environments, CloudSat provides a valuable perspective on the convective process itself, rather than only the precipitation process.

In this study, we compare CloudSat observations from 30 January to 28 February 2007, with DYAMOND simulations for the same period in 2020. We use the 2007 data for CloudSat because although it was launched on 28 April 2006, it experienced a battery anomaly in April 2011, which led to its temporary exit from the A-Train constellation. Subsequently, CloudSat drifted away from the A-Train for about 6 months while a new operations plan was being implemented. In November 2011, CloudSat transitioned to "Daylight Only Operations" mode, allowing it to continue collecting cloud radar data only during sunlit portions of its orbit, hence nighttime (a.m.) data are only available until 2010 (Nayak, 2012). In addition, between 5 July 2019, and 26 August 2020, satellite pointing or timing errors caused surface heights in radar profiles to mismatch the Digital Elevation Map (DEM). This issue makes it difficult to compare even the daytime-only data with the DYAMOND simulations. Also, our previous results (Takahashi et al., 2024) suggest that the characteristics of convection may change during El Niño and La Niña: convection observed during El Niño tends to have broader cores and lower entrainment rates, translating to greater intensity compared to La Niña. This pattern was consistent across all three major tropical "chimney zones." Hence, to better align atmospheric conditions with those of 2020, we selected 2007 for our study. January–February 2020 exhibited weak El Niño conditions, similar to the moderate El Niño conditions of 2007. This selection was in contrast to the strong to moderate La Niña conditions of 2008–2009 and the strong El Niño conditions of 2010.

2.2. DYAMOND Simulations

We evaluate four model simulations produced for DYAMOND Winter (Phase-II, https://www.esiwace.eu/the-project/past-phases/dyamond-initiative/services-dyamond-winter), which include X-SHiELD 3.0 km, GEOS

Table 1
Summary of DYAMOND Model Descriptions

Model	Name	Institution	Resolutions	Experiments
X-SHiELD	eXperimental System for High-resolution prediction on Earth-to-Local Domains	National Oceanic and Atmospheric Administration (NOAA), USA	3.0 km	Atmosphere-only
GEOS	Goddard Earth Observing System	NASA's Goddard Space Flight Center (NASA/GSFC), USA	3.0 km 1.5 km	Coupled Atmosphere-only
IFS	Integrated Forecasting Model	European Centre for Medium-Range Weather Forecasts (ECMWF), UK	4.0 km	Coupled

1.5 km, GEOS 3.0 km, and IFS 4.0 km. These models provide cloud hydrometeor outputs available via the DYAMOND data server, which are necessary inputs for generating reflectivity profiles in dBZ using a CloudSat simulator (Haynes et al., 2007; Hogan & Battaglia, 2008). This allows for a direct comparison with CloudSat observations, as the simulator accounts for attenuation and multiple scattering, ensuring comparable attenuation sensitivity between the model-generated and observed reflectivity. Details of the satellite simulator used in this study are provided in Section 2.3. Further, to ensure a fair comparison between the simulation results and CloudSat observations —given that CloudSat cannot capture the full diurnal cycle, we use only a subset of the DYAMOND models that align with the CloudSat orbit from 30 January to 28 February 2007. For each model, we select grid points closest to each individual CloudSat footprint, creating a one-to-one matchup between CloudSat and each DYAMOND simulation, with data from both CloudSat and DYAMOND simulations occurring at 1:30 a.m./p.m local times. This approach ensures consistent sampling across models and observations. Although the DYAMOND Winter phase runs from 20 January to 1 March 2020, we restrict our analysis to 30 January to 28 February 2020, with the prior 10 days excluded as a spin-up period. The specifications of these models are summarized in Table 1.

2.3. CloudSat Simulator

Radar reflectivity values consistent with the 94 GHz CloudSat radar are simulated for each of the DYAMOND data sets using the Passive-Active Microwave Simulator (PAMS), an extension of the widely used Quickbeam simulator (Haynes et al., 2007), updated to include multiple scattering using the method described by Hogan and Battaglia (2008). Liquid (cloud and rain) scattering is modeled using Mie theory, while ice scattering can be approximated using two different approaches. The first uses an offline database of scattering properties computed for a diverse set of ice crystal monomers, (unrimed) aggregates, graupel, and hail computed using a discrete dipole approximation (DDA; Eriksson et al., 2018). The second approach uses the self-similar Rayleigh-Gans approximation (SSRGA; Hogan et al., 2017; Ori et al., 2021) to represent aggregates with varying degrees of accumulated rime.

Particle size distributions (PSDs) are represented consistent with the assumptions used in each model's cloud microphysics scheme. Ice scattering properties were set to a consistent set for each simulation that, in testing, were demonstrated to yield the best global fit to the CloudSat observations. Specifically, pristine ice was assumed to be comprised of plates, snow was assumed to consist of large plate aggregates, and (where available) graupel was specified to have moderate density. Specific descriptions of each category can be found in Eriksson et al. (2018).

3. Methodologies

3.1. Deep Convective "Cores" and Proxies of Convective Strength

We begin by screening radar profiles using a criterion of reflectivity ≥ -30 dBZ to detect hydrometeors (Bacmeister & Stephens, 2011; Riley & Mapes, 2009), thereby identifying clouds. Among these clouds, we identify deep convective cores (DCCs) based on profiles that meet two conditions: (1) a continuous radar echo (i.e., hydrometeors) extends from the cloud top to within 2 km of the surface, indicating that the cloud is rooted in the planetary boundary layer, and (2) an echo top height (ETH) of 10 dBZ that reaches or exceeds 10 km, suggesting the cloud has strong enough updrafts to loft precipitation-sized particles to this altitude in turn producing these higher reflectivities. Occurrence frequencies of DCCs over the tropics are illustrated in Figure 1 and summarized in Table 2 for both CloudSat observations and the four DYAMOND simulations

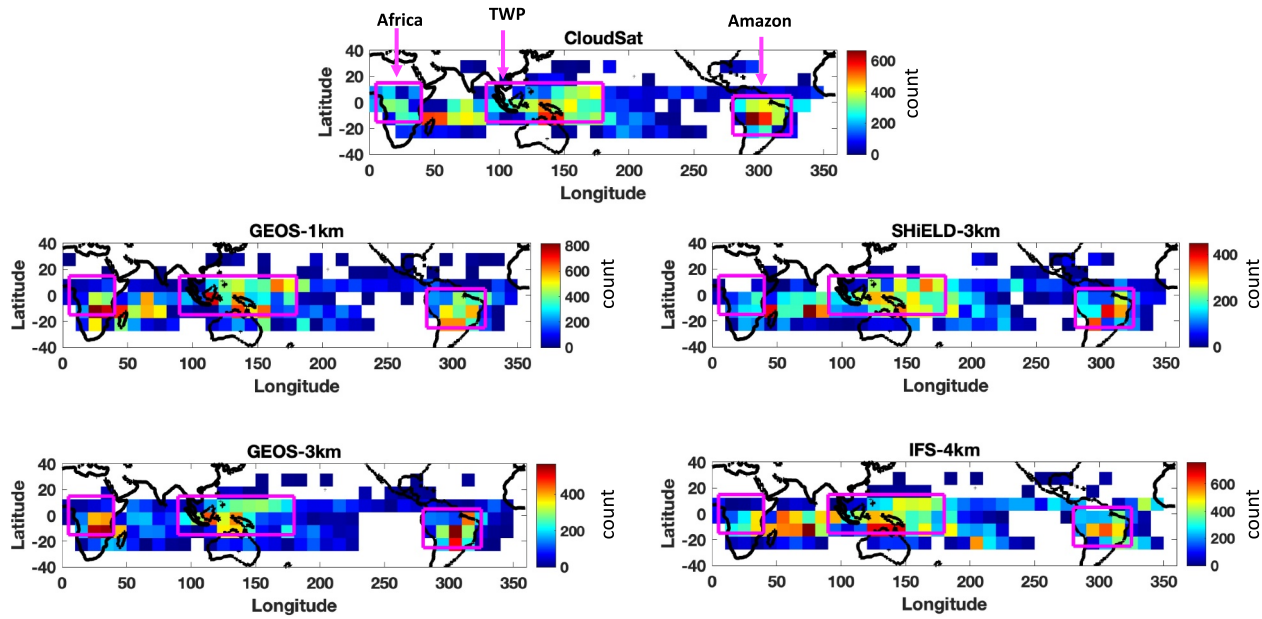

Figure 1. Distribution of sample size (total number) for DCCs based on CloudSat observations and DYAMOND simulations in 10° × 10° boxes over the whole tropics (30°S–30°N). Magenta solid boxes define the three selected regions discussed in the text: Tropical Africa (5°–40°E, 15°S–15°N), Tropical Amazonia (80°–35°W, 25°S–5°N), and the Tropical Warm Pool (TWP, 90°–180°E, 15°S–15°N).

studied. As expected, DCCs are more concentrated over the three 'chimney zones' being over the region of the Amazon, Africa and the tropical west Pacific (TWP) than over the eastern Pacific ITCZ. It is interesting to point out that the area close to Madagascar also becomes a regional hotspot. This region is recognized for experiencing intense tropical depressions during January and February that sometimes escalate into tropical cyclones (Mavume et al., 2009; Rapolaki & Reason, 2018), a phenomenon linked to the high values of low-level moist static energy (MSE) in the area (Hart et al., 2019).

For each DCC, we compute four proxies for convective strength used in previous studies (e.g., Takahashi et al., 2017; Takahashi & Luo, 2014). The first proxy is the ETH of large radar echoes. Specifically, ETH at 0 dBZ and 10 dBZ represents the highest altitude at which 0 dBZ and 10 dBZ radar echoes, respectively, are detected. A strong updraft tends to produce high ETH values, indicating that large particles are being lofted to greater altitudes. It is important to note that the attenuation of radar reflectivity is negligible when identifying the highest levels of 10 dBZ and 0 dBZ echoes from the cloud top downward; for deep convective clouds, these high ETH values are typically found near the cloud top, well above the melting levels. The second proxy, cloud top-echo top distance (CTETD), is defined as the vertical distance between the cloud top height (CTH) and ETH of either 0 dBZ or 10 dBZ, where CTH closely corresponds to ETH of −30 dBZ. Strong convection results in small CTETD values because both small and large particles are together lofted to higher altitudes, making CTH and ETH similar. Conversely, weak convection leads to large CTETD values as large particles do not reach the cloud top. Since existing satellites, including CloudSat observations, have no direct measurement of convective strength, we use these four proxies (ETH0dBZ, ETH10dBZ, CTETD0dBZ, and CTETD10dBZ) to explore the dynamics of DCCs.

Table 2
Total Number of DCC Over the Three Regions

	CloudSat	GEOS-1km	GEOS-3km	SHiELD-3km	IFS-4km
Tropical Africa	1,524	2,196	1,691	694	1,834
Tropical Amazonia	3,402	3,993	2,778	1,907	3,338
TWP	6,080	5,903	3,774	4,311	6,956

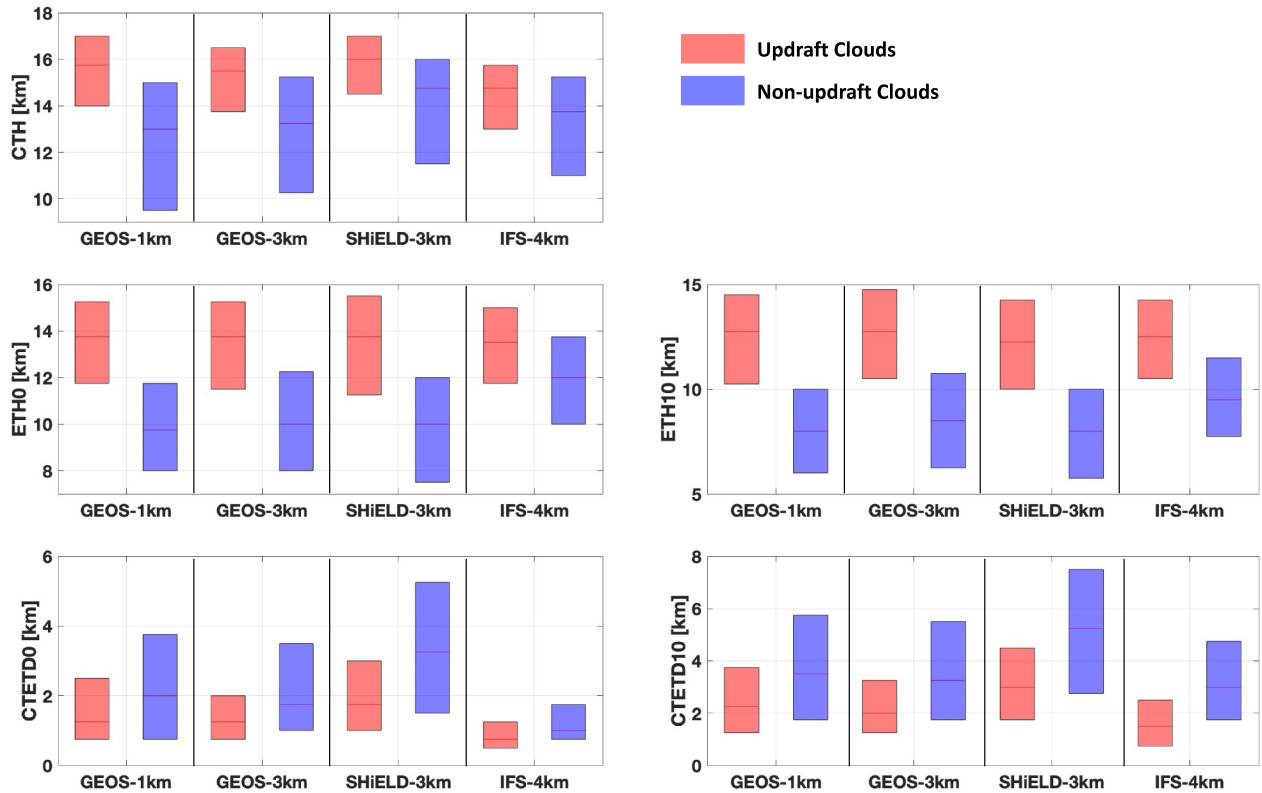

Figure 2. Box diagrams for CTH and the four proxies for convective strength over updraft clouds (red boxes) and non-updraft clouds (blue boxes) for the DYAMOND simulations. The bottom and top of the boxes show, respectively, the 25% and 75% percentile, and the central lines show the medians.

3.2. Updraft Versus Non-Updraft Cores in the DYAMOND Simulations

We cannot directly measure or infer vertical velocity from CloudSat observations, which is why the four proxies of convective updrafts were introduced. Since the DYAMOND simulations provide vertical velocity information, we can distinguish updrafts from downdrafts and assess how well the four observational proxies identify the presence of cores and differentiate between updraft and non-updraft cores. In the model simulations we define an updraft to exist when a vertical velocity of at least 1 m/s is sustained across four contiguous vertical bins of 250 m each above an altitude of 5 km. As Figure 2 confirms, all the DYAMOND simulations show that CTH, ETH0dBZ, and ETH10dBZ are higher in updrafts, whereas CTETD0dBZ and CTETD10dBZ are smaller for updraft clouds compared to non-updraft clouds. These results enhance our confidence in using the four proxies as indicators of convective strength.

All four proxies have some degree of association with magnitudes of vertical intensity of DCCs, but the relationships are not linear and do not exhibit a one-to-one correspondence with updraft velocity. This means that while stronger updrafts tend to result in higher ETH and lower CTETD values, variations in microphysical conditions and cloud structure can lead to deviations from this general pattern. Therefore, the combination of these proxies provides a more comprehensive picture of convective dynamics, but further investigation is needed to better understand how each proxy reflects the complex interplay between updraft intensity, microphysical processes, and cloud structure.

3.3. Environmental Dependences

To link the convective characteristics to buoyancy, we examine the difference between the virtual temperature of an air parcel (Tp) and the environmental virtual temperature (Te), represented as $Tp-Te$, as a function of height (Lucas et al., 1994). Understanding the $Tp-Te$ profile is crucial, as it reveals the vertical buoyancy structure and helps assess the potential intensity of convection. Where $Tp-Te$ is positive, the air parcel is warmer and more buoyant than the surrounding environment, allowing it to rise. This process begins at the Level of Free Convection

(LFC), where the $Tp-Te$ value first becomes zero at a lower level, and continues to be positive until the parcel reaches the Level of Neutral Buoyancy (LNB), where $Tp-Te$ again becomes zero. At the LNB, the parcel's temperature matches that of the surrounding environment, and its buoyancy becomes neutral. Integration of the positive $Tp-Te$ region between the LFC and LNB represents Convective Available Potential Energy (CAPE), which indicates the energy available for the parcel to rise and be accelerated upward. Takahashi et al. (2023) also demonstrated that examining the $Tp-Te$ profile diagrams provides a more meaningful comparison of regional differences than relying solely on a single CAPE value. Note that both the LNB and CAPE here are derived from parcel theory, so the description is idealized and does not account for mixing or entrainment effects. According to parcel theory, the extent to which actual convective development (e.g., CTH) falls short of the LNB set by the ambient sounding reflects the magnitude of entrainment: greater entrainment leads to a larger difference between LNB and CTH resulting from a loss of parcel buoyancy when entraining cooler dry air from outside the core. Hence, the difference between LNB and CTH suggest the magnitude of entrainment dilution.

To estimate Tp, we assume pseudoadiabatic ascent from the planetary boundary layer. To account for the uncertainty associated with the originating level, we launch the air parcel from both the surface and the level having the maximum MSE between the surface and 925 hPa, following Liu and Zipser (2005). The results presented are based on the latter method. Note that for the observation, Tp is estimated by ECMWF-AUX, which originally has a 50-km resolution but is interpolated in space and time to match the CloudSat track. To ensure a fair comparison with each DYAMOND simulation, all Tp and Te values based on DYAMOND data sets are interpolated to the same 50-km resolution.

4. Results and Interpretations

To conduct a fair comparison between the CloudSat observations and the DYAMOND simulations, the CloudSat observations (originally at ∼1 km spatial scale) were interpolated to ∼4 km by averaging three observation pixels. As this did not produce any significant difference from results obtained assuming the native CloudSat resolution (Figures S1 and S2 in Supporting Information S1), we use the original resolution in the analysis described below. This suggests that the resolution mismatch between the DYAMOND simulations and CloudSat observations is not the primary cause of the differences in their results, and that the discrepancies among the models are more likely related to differences in model physics.

4.1. The Environment

The most continental (i.e., Tropical Africa) to most oceanic (i.e., TWP) environment is visualized in Figure 3 by the $Tp-Te$ profile diagrams, and the results of CloudSat presented this way are consistent with those in Takahashi et al. (2023). As described in Section 3.3, the $Tp-Te$ diagram not only illustrates the vertical buoyancy profile but also provides key information about the LFC, LNB, and CAPE. The LFC and LNB are the points where the $Tp-Te$ values are zero at the lowest and highest altitudes, respectively. Integrating the positive $Tp-Te$ region from the LFC to the LNB yields the CAPE, while the difference between the LNB and the CTH indicates the extent of entrainment dilution.

The LNB is found to be highest over the TWP, followed by the Tropical Amazonia, and then Tropical Africa, while the LFC is highest over Tropical Africa, followed by the Tropical Amazonia, and then the TWP. CAPE is slightly higher over the TWP due to the highest LNB and lowest LFC, with similar shapes of the vertical buoyancy profiles among the three tropical chimney regions.

Compared to ECMWF-AUX, the shapes of the $Tp-Te$ profiles vary significantly among the DYAMOND models, highlighting key differences in their vertical buoyancy profiles. For instance, the SHiELD-3km environment features only a shallow layer of positive buoyancy, with an extremely low LNB between 6 and 8 km. This suggests that convective development is limited in altitude, likely affecting storm intensity and the overall depth of convection in this model. By contrast, IFS-4km exhibits a more top-heavy buoyancy profile, with positive buoyancy extending higher into the atmosphere, resulting in a relatively elevated LNB above 16 km. Among the DYAMOND models, the GEOS environment most closely matches to ECMWF-AUX capturing the general shape of the buoyancy profile and the positioning of the LNB and LFC, which is critical for accurately representing the initiation and depth of convection.

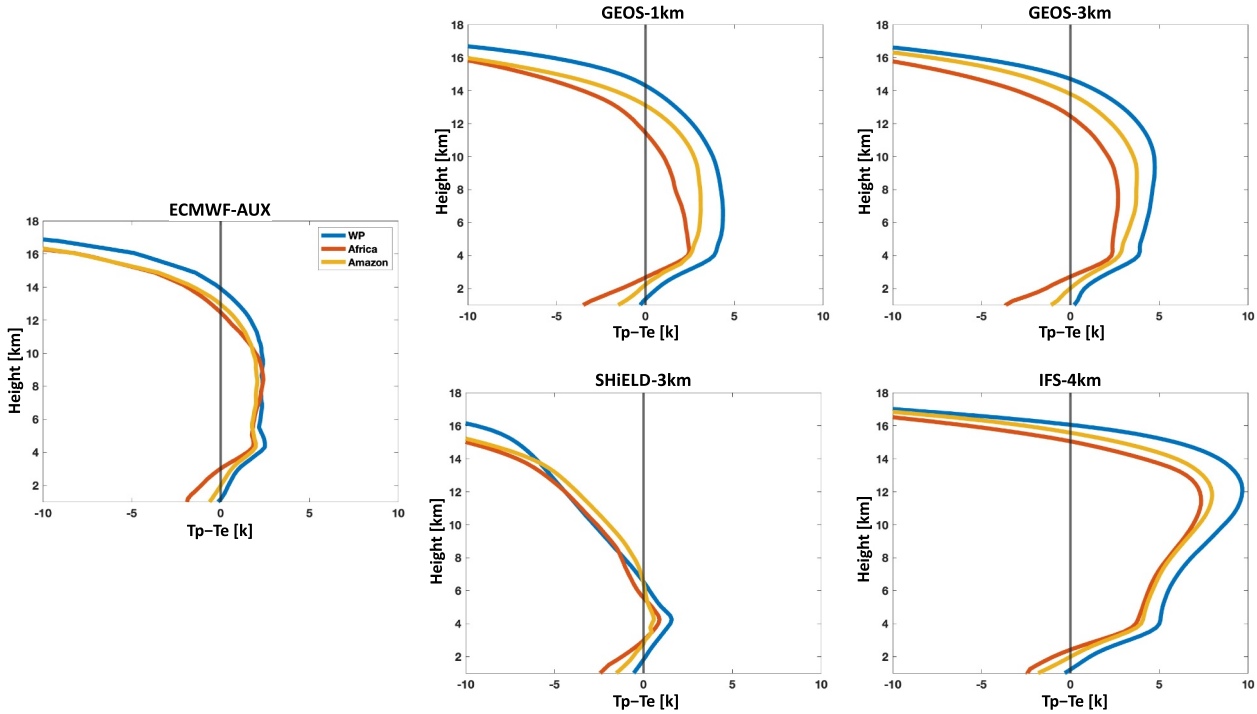

Figure 3. Mean virtual temperature of an air parcel (*Tp*) minus environmental virtual temperature (*Te*) under pseudoadiabatic ascent for Tropical Warm Pool (blue), Tropical Africa (red) and Tropical Amazonia (yellow) for ECMWF-AUX and the DYAMOND simulations.

However, the most intriguing comparison in Figure 3 lies in the contrast among the three regions; the order of highest to lowest LFC, LNB, and CAPE is the same between observations and the DYAMOND models. This indicates that despite some biases in the DYAMOND simulations, the environmental differences among the three regions are generally representing the environment changes observed from region to region.

It is again interesting to point out that the SHiELD-3km model deviates significantly from observations in terms of its buoyancy profile. The shallow layer of positive buoyancy and low LNB point to potential deficiencies in how the model represents convective dynamics, likely resulting in weaker vertical velocities. In contrast, the higher LNB in IFS-4km suggests stronger vertical motion. This makes it particularly interesting to compare the convective strength between DYAMOND simulations and observations, as well as among the three regions.

4.2. Proxies for Convective Strength

The four proxies for convective strength as well as CTH for CloudSat observations and the DYAMOND simulations are summarized in Figure 4. While the *Tp*−*Te* profiles imply that IFS-4km should exhibit the highest CTH and SHiELD-3km the lowest among the DYAMOND models, this is not supported by the simulated CTH values. Instead, IFS-4km shows CTH values comparable to, or slightly lower than, those in GEOS-1km and GEOS-3km. Unexpectedly, SHiELD-3km produces the highest CTH, despite environmental conditions indicating a low LNB between 6 and 8 km. One possible explanation is that convection can significantly alter its surrounding environment. Overactive convection in the model may rapidly deplete CAPE, leading to a more stable atmospheric state. As a result, there may be a temporal offset between the onset of intense convection and the corresponding CAPE values. Future investigations should attempt a full interpretation of the connections between convective CTH and low-buoyancy profiles.

We now turn to regional comparisons of the proxies and CTH. According to Student's *t*-test results, the differences between Tropical Africa and the TWP are statistically significant at the 95% confidence level for both CloudSat and the DYAMOND simulations, with p-values near zero for all proxies except for the ETH10dBZ in SHiELD-3km.

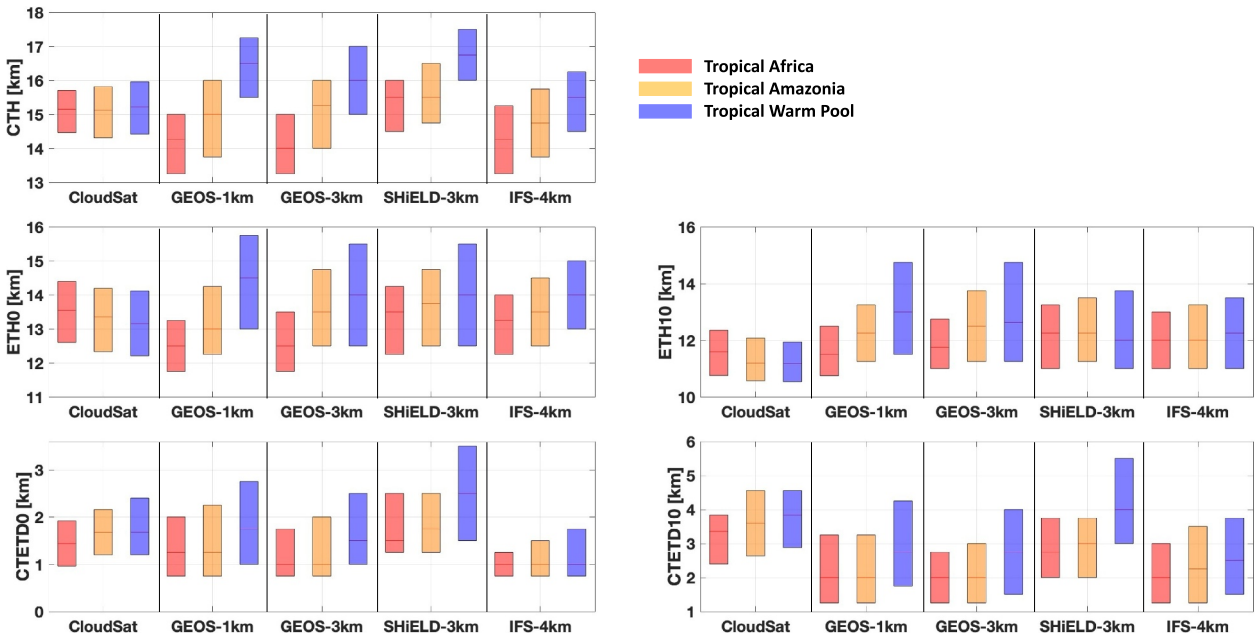

Figure 4. Box diagrams for CTH and the four convective strength proxies from CloudSat observations and the DYAMOND simulations in DCCs over the three convective regions: Tropical Africa (red boxes), Tropical Amazonia (orange boxes) and the Tropical Warm Pool (blue boxes). The bottom and top of the boxes show, respectively, the 25% and 75% percentile, and the central lines show the medians.

Previous studies (Cecil et al., 2014; Liu et al., 2007; Takahashi et al., 2023; Zipser et al., 2006) suggest that convective intensity is strongest over Tropical Africa, followed by the Tropical Amazonia and TWP. This pattern of convective intensity is also reflected in the one month of CloudSat data analyzed: ETH0dBZ and ETH10dBZ are highest over Tropical Africa, followed by the Tropical Amazonia, and then the TWP, while CTETD0dBZ and CTETD10dBZ are shortest over Tropical Africa, followed by the Tropical Amazonia, and then the TWP. It is noteworthy that, although ETH and CTETD vary across different regions, CTH is relatively similar in the CloudSat analysis (Figure 4). This means that the difference between the LNB and CTH reaches their highest values over TWP, with the Tropical Amazonia and Tropical Africa following in descending order. The difference between the LNB and CTH can be interpreted as the magnitude of convective dilution due to entrainment effects on the DCCs. This is because LNB represents the idealized cloud top height that a cloud could achieve in the absence of entrainment, where no interaction occurs between the air parcel and its surrounding environment. On the other hand, CTH is the actual cloud top height, reflecting the impact of entrainment. In reality, convective entrainment reduces buoyancy, preventing the cloud from reaching its LNB. Therefore, the largest difference between the LNB and CTH over the TWP implies a greater entrainment effect on the DCCs compared to other regions. The CloudSat observations suggest that the DCCs are more intense over Tropical Africa and comparatively less intense over the TWP due to smaller and larger entrainment effects, respectively.

Unlike the CloudSat observations, the CTH varies among regions in the DYAMOND simulations, consistently showing the highest CTH over the TWP, followed by Tropical Amazonia, and then Tropical Africa (Figure 4). The results of the four proxies for convective strength also vary across the DYAMOND models. To better interpret the results, the mean and maximum updraft speeds of DCCs in the three regions are examined and summarized in Table 3. It may seem surprising that the mean updraft speeds for DCCs are quite low (typically around 3–5 m/s). DYAMOND simulations tend to produce very low vertical velocities, a finding that has also been reported in other multiscale modeling frameworks (e.g., Dodson et al., 2018).

In both the GEOS-1km and GEOS-3km simulations (Figure 4), ETH0 and ETH10dBZ rank the regions similarly to CTH. In the SHiELD-3km and IFS-4km simulations, ETH0dBZ also ranks the regions similarly to CTH, but ETH10dBZ shows small differences among the regions. For CTETD0 and CTETD10dBZ, all the DYAMOND simulations show the same regional ranking as CloudSat. However, unlike CloudSat, which shows relatively uniform CTH across the regions, the DYAMOND simulations exhibit substantial regional variations in CTH. As a result, the interpretation of CTETD0 and CTETD10dBZ in the DYAMOND simulations may differ from those

Table 3
Mean and Maximum Updraft Speeds [m/s] of DCCs Across the Three Regions in DYAMOND Simulations

Mean (Max) V [m/s]	GEOS-1km	GEOS-3km	SHiELD-3km	IFS-4km
Tropical Africa	0.82 (23.06)	0.88 (21.05)	0.80 (23.35)	0.35 (14.29)
Tropical Amazonia	0.92 (41.05)	0.87 (28.14)	0.87 (20.48)	0.38 (15.64)
TWP	1.04 (40.48)	0.94 (31.72)	0.66 (23.30)	0.37 (15.47)

based on CloudSat, leading to mixed interpretations of convective strength. Thus, when we focus on results based on CTH, ETH0, and ETH10, overall results suggest that although convection is most intense over Tropical Africa in reality (as observed by CloudSat), the DYAMOND simulations tend to produce the deepest and most intense convection over the TWP, followed by Tropical Amazonia and then Tropical Africa. This pattern is particularly pronounced in the GEOS-1km and GEOS-3km simulations, whereas ETH10dBZ shows relatively small differences for SHiELD-3km and IFS-4km. This discrepancy may be linked to the higher LNB over the TWP (Figure 3), which can favor stronger vertical motion, as GEOS-1km and GEOS-3km both exhibit higher mean updraft speeds over the TWP compared to the other two regions. In contrast, SHiELD-3km shows the weakest updrafts over the TWP, while IFS-4km displays mean updraft speeds that are similar across the three regions.

4.3. Internal Vertical Structure

An alternative approach to investigate convective intensity involves examining the internal vertical structure through the Contoured Frequency by Temperature Diagram (CFTD; Hashino et al., 2013; Takahashi et al., 2017). The CFTD is similar to the Contoured Frequency by Altitude Diagram (CFAD; Yuter & Houze, 1995), a widely-used method for statistically characterizing radar reflectivity as a function of altitude. CFADs show the frequency of occurrence of reflectivity values at different heights for the total sample of deep convective clouds analyzed in this study. Data are binned into dBZ intervals at each height level and then normalized by the total number of samples at that level. However, CFAD can inadvertently mix temperatures when binning radar echoes by altitude, potentially obscuring the underlying relationships, as radar reflectivity is closely tied to cloud water content, which is strongly influenced by temperature (Fridlind et al., 2015). To address this issue, Hashino et al. (2013) and Takahashi et al. (2017) proposed the CFTD as an alternative metric that organizes radar echoes by temperature.

Following Takahashi et al. (2017), we aim to gain a clearer understanding of convective intensity across different regions by comparing two convective regimes: tropical land regions (Tropical Africa and Amazonia combined, Figure 5, top panels) and the TWP (Figure 5, middle panels). For CloudSat observations, both tropical land regions and the TWP exhibit a "inverse-C"-shaped pattern in CFTD: reflectivity increases with increasing temperature (indicating smaller particles at cloud tops or higher altitude), but then rapidly decreases below the melting layer due to attenuation from heavy precipitation. Also, two distinct features stand out in CloudSat observations of the land-ocean contrast (Figure 5, bottom panels): continental DCCs exhibit a higher frequency of larger radar echoes (>10 dBZ) at colder or higher altitudes (marked as a dark solid oval), and attenuation due to heavy precipitation is more pronounced in continental DCCs compared to oceanic ones (marked as a dark dashed oval). Both the larger radar echoes at higher altitudes and the more severe attenuation at lower altitudes are consistent with more intense DCCs over land. This is because stronger convective motions are more capable of transporting larger particles to higher levels and generating heavier rainfall. The four proxies of convective strength derived from CloudSat suggest that convection is most intense over Tropical Africa, followed by the Tropical Amazonia, and then the TWP (Figure 4). Hence, the results of the CFTD analysis align with these expectations.

Note that tropical deep convection over land exhibits a pronounced diurnal cycle, typically peaking in the late afternoon (Liu & Zipser, 2008). This means that CloudSat likely underestimates the frequency of DCCs over land because its overpasses occur around 1:30 a.m./p.m local time. Since CloudSat misses the peak stage of convective activity over land, the contrast between Tropical Africa and the TWP in Figure 4 or the contrast between the tropical land regions and the TWP in Figure 5 can be even larger, as our samples of continental intensity are biased toward weaker magnitudes. In contrast, deep convection over the ocean shows a much weaker diurnal cycle (Liu & Zipser, 2008), so the underestimation is expected to be less significant over the ocean.

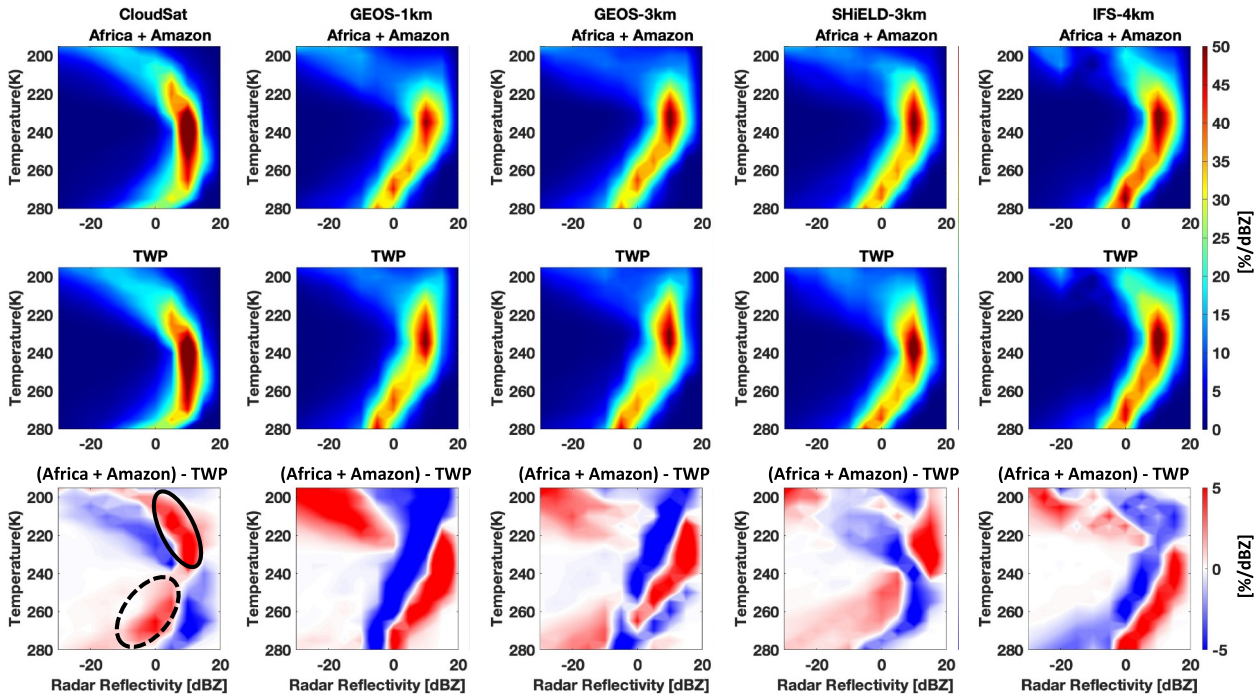

Figure 5. Contoured frequency by temperature diagrams (CFTDs) for DCC over (top) the two tropical land regions (Tropical Africa and Amazonia), (middle) the Tropical Warm Pool, and (bottom) the difference between them for CloudSat observations and the DYAMOND simulations.

Unlike CloudSat observations, the DYAMOND-simulated radar profiles do not have the "inverse-C" shape. This suggests that all the DYAMOND simulations tend to produce significantly heavier precipitation at higher altitudes than CloudSat observations, as their radar attenuation begins at relatively colder temperatures or higher altitudes compared to CloudSat observations.

It is interesting to point out that the land-ocean contrast in the CFTD of DYAMOND simulations also differs significantly from CloudSat observations, except SHiELD-3km. As shown in earlier results based on ETH-derived convective proxies and *Tp–Te* profile diagrams, the DYAMOND models consistently suggest that the strongest convection occurs over the TWP among the three tropical regions. This is further reflected in the land–ocean contrast patterns for GEOS-1km and IFS-4km, where the TWP exhibits a higher frequency of larger radar echoes at colder temperatures or higher altitudes. Moreover, attenuation due to heavy precipitation appears more prominently over the TWP than over the tropical land regions.

Surprisingly, SHiELD-3km exhibits a pattern that closely resembles CloudSat observations warmer than 210 K. However, colder than 210 K, SHiELD-3km shows a higher frequency of larger radar echoes over the TWP compared to the two tropical land regions, unlike the pattern observed in CloudSat data. For GEOS-3km, the land–ocean contrast in CFTD shows a mixed pattern. Similar to GEOS-1km and IFS-4km, GEOS-3km also shows a higher frequency of larger radar echoes at colder temperatures or higher altitudes. However, attenuation due to heavy precipitation (e.g., warmer than 270 K) is more evident in the two tropical land regions than in the TWP, similar to CloudSat and SHiELD-3km.

5. Uncertainty and Sensitivity Tests

5.1. Sensitivity to Uncertainty in Ice Crystal Habit

Since we use a forward model (the Passive-Active Microwave Simulator; PAMS) to generate radar reflectivity values consistent with the 94 GHz CloudSat radar, it is important to understand the effects of uncertainties in the simulator assumptions. One of the key assumptions made in radar forward models pertains to the shapes and densities of ice crystals. To evaluate the sensitivity of our results to changes in these assumptions, we conduct PAMS ice scattering sensitivity experiments. Specifically, we assess how variations in ice and snow density, ranging from denser to less dense forms, affect the simulated reflectivity. Our default settings assumed that

pristine ice was comprised primarily of short columns, consistent with observations in tropical convective cirrus clouds, with larger ice (snow) comprised of longer (deposition-grown) columns. These lie at the higher-density end of the spectrum of ice habits observed in nature. To test sensitivity to particle density, we replaced the pristine ice category with a longer and narrower (overall less dense in terms of the circumscribed sphere) ice column scatterer. We replaced the larger ice (snow) category with a lightly rimed aggregate. As with the pristine ice category, this is less dense than the original.

The experiments indicate that heights of cloud tops and echo tops such as ETH0dBZ and ETH10dBZ, increase slightly (less than 1.5 km) when less dense ice/snow is used, leading to a corresponding small upward shift in the CFTD. This behavior arises because lower-density hydrometeors exhibit reduced scattering efficiency, resulting in lower reflectivity at a given altitude and thereby elevating the height thresholds at which specific reflectivity values are reached. However, the primary focus of this study is to examine regional contrasts among Tropical Africa, Tropical Amazonia, and the TWP. The differences in simulated reflectivity across these regions remain broadly consistent despite variations in ice/snow density (Figures S3, S4, and S5 in Supporting Information S1), and thus do not significantly affect our overall results.

5.2. Sensitivity to Sampling

In addition, due to the relatively short duration of the DYAMOND simulation period, the sample size is limited, making it necessary to assess potential uncertainties in both the model and observational-based results. First, to evaluate the influence of limited sampling on DYAMOND-based analyses, we employ the GEOS-3km simulation to generate full-domain reflectivity fields at 1:30 a.m./p.m local time across a 30-day period. This approach increases the sample size of DCCs by approximately 700-fold, yielding 1196,601 DCCs over Tropical Africa, 2157,608 over the Tropical Amazon, and 2514,335 over the TWP. Such enhancement allows us to evaluate how results differ when only a CloudSat orbit subset of DYAMOND model locations are used, compared to full coverage. Although the absolute heights of cloud tops and echo tops differ, the regional contrasts in these variables as well as in the difference of CFTD remain consistent (Figures S6 and S7 in Supporting Information S1). As a result, these differences also do not significantly influence our overall findings.

5.3. Sensitivity to Comparing CloudSat's 2007 to DYAMOND's 2020

Finally, to evaluate the robustness of our observation-based findings, we first compared the 2007 CloudSat results with the 2006–2010 climatology reported in previous studies (e.g., Figures 1b, 1c, and 2b of Takahashi et al., 2023, and Figure 6 of Takahashi et al., 2017). This comparison indicates that the land–ocean differences across the three tropical chimney zones are consistently represented from year to year. Although some absolute values differ, particularly under varying ENSO phases, the qualitative contrast between land and ocean convection remains remarkably stable. Therefore, we maintain that focusing on 30 January–28 February in 2007 allows for a meaningful and representative comparison with the same dates in 2020, especially given the moderate El Niño conditions in both years. This careful selection helps minimize potential biases due to interannual variability and supports the robustness of our conclusions, which emphasize the spatial structure of convection rather than precise year-to-year magnitudes.

6. Discussions and Summary

Tropical deep convective cores (DCCs) and their surrounding environments are compared between CloudSat observations and DYAMOND simulations, over three major tropical "chimney zones" (Tropical Africa, Tropical Amazonia, and the Tropical Western Pacific). Despite some biases in the DYAMOND simulations, the environmental differences among the three regions are generally well captured, except in the SHiELD-3km simulation. However, further investigation of convective intensity, based on proxies for convective strength and CFTD, suggests that the DYAMOND simulations do not accurately replicate the patterns observed. This indicates that, although the simulations successfully reproduce similar thermodynamic conditions, they do not adequately capture their connection to convective dynamics and processes. As a result, the DYAMOND simulations tend to overestimate CTH, ETH0dBZ, and ETH10dBZ over the TWP and underestimate them over Tropical Africa. To facilitate clearer interpretation, we provide additional summary figures (Figure 6) that depict the median values of CTH versus ETH0dBZ and CTH versus ETH10dBZ for CloudSat and the DYAMOND simulations across the three tropical regions. These summary plots reveal that CloudSat data indicate relatively uniform CTH among the

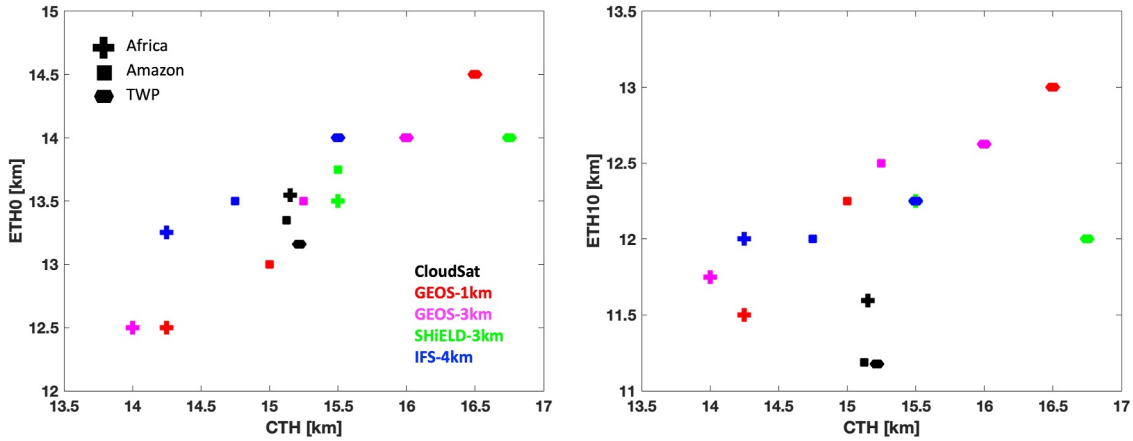

Figure 6. Relationship between (left) CTH and ETH0dBZ, and (right) CTH and ETH10dBZ for CloudSat (black), GEOS-1km (red), GEOS-3km (magenta), SHiELD-3km (green), and IFS-4km (blue) over the three regions.

regions, whereas the DYAMOND simulations exhibit a distinct gradient, with the highest CTH over the TWP, followed by Tropical Amazonia, and the lowest over Tropical Africa.

Furthermore, the CTH–ETH0 and CTH–ETH10 relationships in the DYAMOND simulations follow a more systematic, linear progression from Tropical Africa to the TWP. In contrast, CloudSat observations show a less pronounced vertical ordering, with Tropical Africa, Amazonia, and the TWP distributed from top to bottom. These results highlight the tendency of DYAMOND simulations to exaggerate regional contrasts in convective depth relative to observations.

This discrepancy may arise because the process by which potential energy is converted to kinetic energy in the DYAMOND simulations differs from that in reality. Based on the $Tp-Te$ diagrams (Figure 3), both observations and simulations show that CAPE is slightly higher over the TWP due to its highest LNB and lowest LFC, with similar shapes of the vertical buoyancy profiles among the three tropical chimney regions. In reality, only a fraction of CAPE is converted to kinetic energy in convective vertical motion, with this fraction being lower for oceanic convection than for continental convection (Takahashi et al., 2023). Therefore, although the TWP has larger CAPE than the two continental regions, its convective intensity is weaker compared to the two continental regions. However, this is not the case of DYAMOND simulations. For example, in both the GEOS-1km and GEOS-3km simulations, the ranking of CAPE from highest to lowest matches the order of convective intensity across the three regions. This suggests that the conversion efficiency of CAPE to kinetic energy over the TWP may be significantly higher in the GEOS simulations compared to the real world. Consequently, the DYAMOND simulations may not accurately represent the conversion efficiency of CAPE in convective vertical motion.

In addition, it is worth noting that there appears to be a missing link between the dynamics and microphysics. As suggested by the CFTD results (Figure 5), DYAMOND simulations tend to produce significantly more heavy precipitation than CloudSat observations, with precipitation forming at similar or slightly higher altitudes among the models despite very low updraft speeds (Table 3). In reality, for larger hydrometeors to be present at these heights, a substantial vertical velocity would typically be required to push them upward. This raises important questions about how precipitation particles are being transported within clouds and how they reach such altitudes without the expected strong updrafts.

One hypothesis is that while most updrafts in the DYAMOND simulations are relatively weak, some stronger updrafts (~3–5 m/s or occasionally exceeding 5 m/s)—may be lifting clouds to higher altitudes. These updrafts could be contributing to an unrealistic scenario where clouds rapidly develop into precipitation, resulting in a "when it rains, it pours" phenomenon. To test this hypothesis, Figure 7 compares CFTDs associated with stronger DCCs (updrafts >3 m/s) and those with weaker DCCs (updrafts <0.5 m/s). The results confirm that stronger updrafts contribute to unrealistically heavy precipitation, while weaker updrafts contribute little to heavy precipitation—except in the case of SHiELD-3km and IFS-4km.

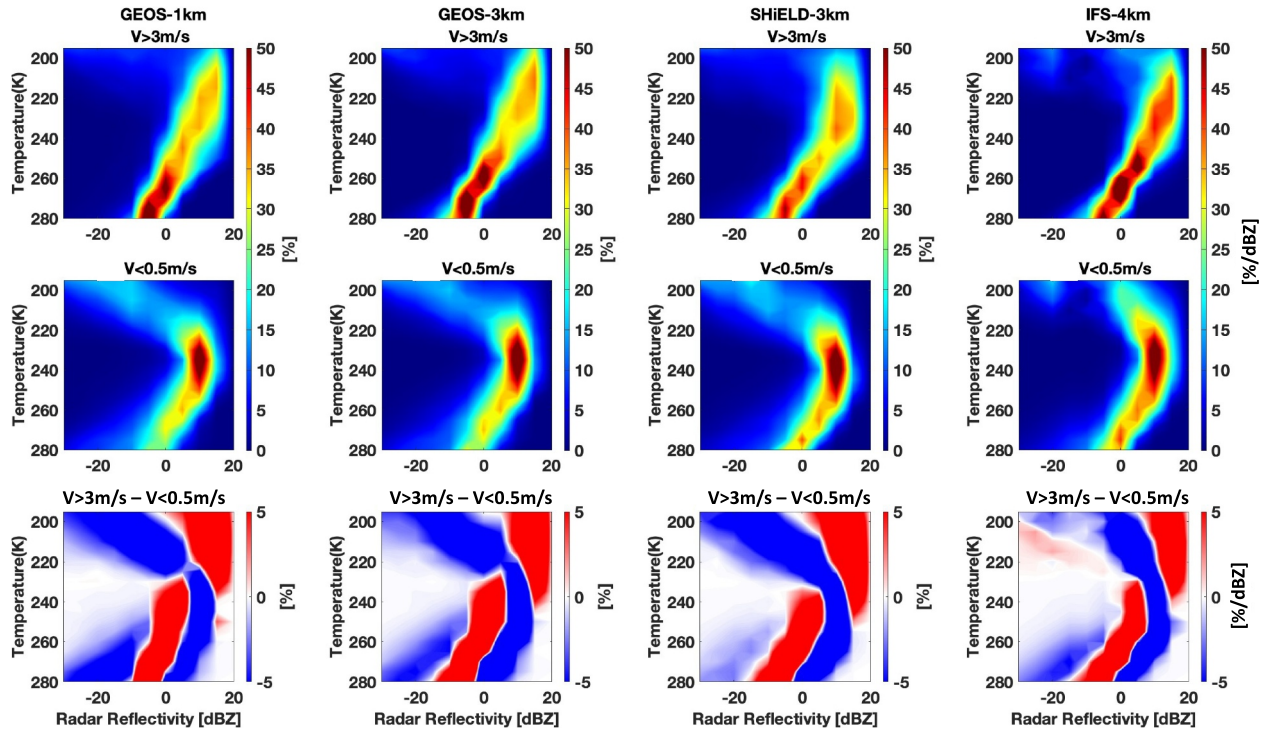

Figure 7. Similar to Figure 5, but for (top) stronger DCC (updrafts >3 m/s), (middle) weaker DCC (updrafts <0.5 m/s), and (bottom) the difference between them for the DYAMOND simulations.

Alternatively, the discrepancy may arise from the fact that, unlike in reality, rain and snow in the simulations are not being carried upward by updrafts from below. Instead, it's possible that clouds formed in the upper layers are quickly converting into precipitation, leading to higher-altitude rain and snow without the usual vertical transport mechanisms seen in nature. This rapid development of precipitation in global models is quite common in warm rain formation processes for shallow clouds (e.g., Stephens et al., 2010; Suzuki et al., 2015), suggesting that similar issues may also arise in the simulation of deep convection. In this scenario, the microphysics of the model may be prematurely converting cloud water and ice into rain or snow, bypassing the natural entrainment and growth processes that typically occur over time. This could explain why the precipitation forms at higher levels despite the low vertical velocities. This discrepancy points to a potential misrepresentation of the relationship between dynamics and microphysics in the DYAMOND simulations. In particular, it raises concerns about how well the models are simulating key processes such as the growth and transport of hydrometeors, as well as the interactions between updrafts and cloud microphysics.

Moreover, physical parameterizations, particularly those for boundary-layer turbulence and shallow convection, are critical for preconditioning the environment that supports deep convection. Thus, part of the discrepancy across models may stem from biases in these parameterizations that are important for the development of deep convection. For instance, SHiELD-3km does not produce a clear land–ocean contrast in updraft speeds when default subgrid parameterizations are used, but such a contrast emerges when the shallow convection scheme is turned off (Abbott et al., 2024). This suggests that SHiELD-3km may generate land–ocean differences in updraft speeds for the wrong reasons, which could be related to the unusual behavior of SHiELD-3km exhibiting the lowest CAPE yet the highest CTH among the DYAMOND simulations. By contrast, IFS-4km shows the highest CAPE and the lowest CTH among the simulations. Previous analyses (Roh et al., 2021) reported that IFS produces a higher fraction of deep and congestus clouds, whereas GEOS yields more high clouds. One possible explanation is that IFS converts cloud water to precipitation less efficiently, allowing more latent heat to remain in the atmosphere and thereby sustaining higher CAPE. It is also interesting to note that the results from GEOS-1km (atmosphere-only) and GEOS-3km (coupled) show no significant differences. This suggests that improvements in model physics can, to some extent, compensate for coarser resolution, such that a coupled simulation at 3 km can produce results comparable to a finer-resolution atmosphere-only run. Further investigation is needed to clarify

these inter-model differences and to better understand how each system represents the interplay between cloud dynamics and precipitation formation.

Conflict of Interest

The authors declare no conflicts of interest relevant to this study.

Data Availability Statement

The data of A-Train observations can be found from the CloudSat Data Processing Center at www.cloudsat.cira.colostate.edu. More specifically, 2B-GEOPROF (Marchand & Mace, 2018) and ECMWF-AUX (Cronk & Partain, 2017) can be found at https://www.cloudsat.cira.colostate.edu/data-products/2b-geoprof and https://www.cloudsat.cira.colostate.edu/data-products/ecmwf-aux, respectively. The DYAMOND data sets (Stevens et al., 2019) can be found from the DYAMOND website at https://easy.gems.dkrz.de/DYAMOND/Winter/index.html.

Acknowledgments
The research was carried out at the Jet Propulsion Laboratory, California Institute of Technology, under a contract with the National Aeronautics and Space Administration (NASA). This study was supported by NASA Grants 80NSSC20K0090 and 80NM0018F058, as well as by INCUS project under Grant 80LARC22DA011. KS was supported by the MEXT program for the Advanced Studies of Climate Change Projection (SENTAN) (Grant JPMXD0722680395) and JAXA/EarthCARE project. DYAMOND data management was provided by the German Climate Computing Center (DKRZ) and supported through the projects ESiWACE and ESiWACE2. The projects ESiWACE and ESiWACE2 have received funding from the European Union's Horizon 2020 research and innovation programme under Grant agreements No 675191 and 823988. This work used resources of the Deutsches Klimarechenzentrum (DKRZ) granted by its Scientific Steering Committee (WLA) under project IDs bk1040 and bb1153. The authors would like to thank Julia Duras, Florian Ziemen, Linjiong Zhou, Thomas Rackow and Peter Dueben for their valuable discussions on utilizing the DYAMOND data set.

References

Abbott, T. H., Jeevanjee, N., Cheng, K. Y., Zhou, L., & Harris, L. (2024). The land-ocean contrast in deep convective intensity in a global storm-resolving model. *Authorea Preprints*.

Bacmeister, J., & Stephens, G. (2011). Spatial statistics of likely convective clouds in CloudSat data. *Journal of Geophysical Research*, *116*(D4), D04104. https://doi.org/10.1029/2010jd014444

Byers, H. R., & Braham, R. R. (1949). *The thunderstorm: Report of the thunderstorm project*. US Government Printing Office.

Cecil, D. J., Buechler, D. E., & Blakeslee, R. J. (2014). Gridded lightning climatology from TRMM-LIS and OTD: Dataset description. *Atmospheric Research*, *135*, 404–414. https://doi.org/10.1016/j.atmosres.2012.06.028

Cronk, H., & Partain, P. (2017). CloudSat ECMWF-AUX auxillary data product process description and interface control document [Dataset]. *Cooperative Institute for Research in the Atmosphere Doc*. https://www.cloudsat.cira.colostate.edu/cloudsat-static/info/dl/ecmwf-aux/ECMWF-AUX_PDICD.P_R05.rev0_.pdf

Dodson, J. B., Taylor, P. C., & Branson, M. (2018). Microphysical variability of Amazonian deep convective cores observed by CloudSat and simulated by a multi-scale modeling framework. *Atmospheric Chemistry and Physics*, *18*(9), 6493–6510. https://doi.org/10.5194/acp-18-6493-2018

Eriksson, P., Ekelund, R., Mendrok, J., Brath, M., Lemke, O., & Buehler, S. A. (2018). A general database of hydrometeor single scattering properties at microwave and sub-millimetre wavelengths. *Earth System Science Data*, *10*(3), 1301–1326. https://doi.org/10.5194/essd-10-1301-2018

Fridlind, A., Ackerman, A., Grandin, A., Dezitter, F., Weber, M., Strapp, J., et al. (2015). High ice water content at low radar reflectivity near deep convection–Part 1: Consistency of in situ and remote-sensing observations with stratiform rain column simulations. *Atmospheric Chemistry and Physics*, *15*(20), 11713–11728. https://doi.org/10.5194/acp-15-11713-2015

Gnitou, G. T., Li, Q., Tan, G., & Nooni, I. K. (2023). Distributional added value analysis of daily CORDEX-CORE RegCM4-7 historical precipitation simulations over Africa. *Atmospheric Research*, *291*, 106818. https://doi.org/10.1016/j.atmosres.2023.106818

Hart, N. C., Washington, R., & Maidment, R. I. (2019). Deep convection over Africa: Annual cycle, ENSO, and trends in the hotspots. *Journal of Climate*, *32*(24), 8791–8811. https://doi.org/10.1175/jcli-d-19-0274.1

Hashino, T., Satoh, M., Hagihara, Y., Kubota, T., Matsui, T., Nasuno, T., & Okamoto, H. (2013). Evaluating cloud microphysics from NICAM against CloudSat and CALIPSO. *Journal of Geophysical Research: Atmospheres*, *118*(13), 7273–7292. https://doi.org/10.1002/jgrd.50564

Haynes, J. M., Marchand, R. T., Luo, Z., Bodas-Salcedo, A., & Stephens, G. L. (2007). A multipurpose radar simulation package: QuickBeam. *Bulletin of the American Meteorological Society*, *88*(11), 1723–1728. https://doi.org/10.1175/bams-88-11-1723

Hogan, R. J., & Battaglia, A. (2008). Fast lidar and radar multiple-scattering models. Part II: Wide-angle scattering using the time-dependent two-stream approximation. *Journal of the Atmospheric Sciences*, *65*(12), 3636–3651. https://doi.org/10.1175/2008jas2643.1

Hogan, R. J., Honeyager, R., Tyynelä, J., & Kneifel, S. (2017). Calculating the millimetre-wave scattering phase function of snowflakes using the self-similar Rayleigh–Gans approximation. *Quarterly Journal of the Royal Meteorological Society*, *143*(703), 834–844. https://doi.org/10.1002/qj.2968

Houze, R. A. (2014). Cloud microphysics. *International Geophysics*, *104*, 47–76. https://doi.org/10.1016/b978-0-12-374266-7.00003-2

Illingworth, A. J., Barker, H., Beljaars, A., Ceccaldi, M., Chepfer, H., Clerbaux, N., et al. (2015). The EarthCARE satellite: The next step forward in global measurements of clouds, aerosols, precipitation, and radiation. *Bulletin of the American Meteorological Society*, *96*(8), 1311–1332. https://doi.org/10.1175/bams-d-12-00227.1

Kummerow, C. (1998). Beamfilling errors in passive microwave rainfall retrievals. *Journal of Applied Meteorology*, *37*(4), 356–370. https://doi.org/10.1175/1520-0450(1998)037<0356:beipmr>2.0.co;2

Kummerow, C., Barnes, W., Kozu, T., Shiue, J., & Simpson, J. (1998). The tropical rainfall measuring mission (TRMM) sensor package. *Journal of Atmospheric and Oceanic Technology*, *15*(3), 809–817. https://doi.org/10.1175/1520-0426(1998)015<0809:ttrmmt>2.0.co;2

LeMone, M. A., & Zipser, E. J. (1980). Cumulonimbus vertical velocity events in GATE. Part I: Diameter, intensity and mass flux. *Journal of the Atmospheric Sciences*, *37*(11), 2444–2457. https://doi.org/10.1175/1520-0469(1980)037<2444:cvveig>2.0.co;2

Liu, C., & Zipser, E. J. (2005). Global distribution of convection penetrating the tropical tropopause. *Journal of Geophysical Research*, *110*(D23). https://doi.org/10.1029/2005jd006063

Liu, C., & Zipser, E. J. (2008). Diurnal cycles of precipitation, clouds, and lightning in the tropics from 9 years of TRMM observations. *Geophysical Research Letters*, *35*(4). https://doi.org/10.1029/2007gl032437

Liu, C., Zipser, E. J., & Nesbitt, S. W. (2007). Global distribution of tropical deep convection: Different perspectives from TRMM infrared and radar data. *Journal of Climate*, *20*(3), 489–503. https://doi.org/10.1175/jcli4023.1

Liu, Z., Ostrenga, D., Teng, W., & Kempler, S. (2012). Tropical rainfall measuring mission (TRMM) precipitation data and services for research and applications. *Bulletin of the American Meteorological Society*, *93*(9), 1317–1325. https://doi.org/10.1175/bams-d-11-00152.1

Lucas, C., Zipser, E. J., & LeMone, M. A. (1994). Vertical velocity in oceanic convection off tropical Australia. *Journal of the Atmospheric Sciences*, *51*(21), 3183–3193. https://doi.org/10.1175/1520-0469(1994)051<3183:vvioco>2.0.co;2

Marchand, R., & Mace, G. (2018). Level 2 GEOPROF product process description and interface control document [Dataset]. *A NASA Earth System Science Pathfinder Mission*. https://www.cloudsat.cira.colostate.edu/cloudsat-static/info/dl/2b-geoprof/2B-GEOPROF_PDICD.P_R04.20070628.pdf

Mavume, A. F., Rydberg, L., Rouault, M., & Lutjeharms, J. R. (2009). Climatology and landfall of tropical cyclones in the south-west Indian Ocean. *Western Indian Ocean Journal of Marine Science*, *8*(1). https://doi.org/10.4314/wiojms.v8i1.56672

Mulholland, J. P., Peters, J. M., & Morrison, H. (2021). How does LCL height influence deep convective updraft width? *Geophysical Research Letters*, *48*(13), e2021GL093316. https://doi.org/10.1029/2021gl093316

Nayak, M. (2012). CloudSat anomaly recovery and operational lessons learned. In *SpaceOps 2012*.1295798

Ori, D., von Terzi, L., Karrer, M., & Kneifel, S. (2021). snowScatt 1.0: Consistent model of microphysical and scattering properties of rimed and unrimed snowflakes based on the self-similar Rayleigh–Gans approximation. *Geoscientific Model Development*, *14*(3), 1511–1531. https://doi.org/10.5194/gmd-14-1511-2021

Rapolaki, R. S., & Reason, C. J. (2018). Tropical storm Chedza and associated floods over south-eastern Africa. *Natural Hazards*, *93*(1), 189–217. https://doi.org/10.1007/s11069-018-3295-y

Riehl, H., & Malkus, J. S. (1958). On the heat balance in the equatorial trough zone. *Geophysica*, *6*, 503–538.

Riley, E. M., & Mapes, B. E. (2009). Unexpected peak near− 15 C in CloudSat echo top climatology. *Geophysical Research Letters*, *36*(9). https://doi.org/10.1029/2009gl037558

Roh, W., Satoh, M., & Hohenegger, C. (2021). Intercomparison of cloud properties in DYAMOND simulations over the Atlantic Ocean. *Journal of the Meteorological Society of Japan. Ser. II*, *99*(6), 1439–1451. https://doi.org/10.2151/jmsj.2021-070

Simpson, J., & Wiggert, V. (1969). Models of precipitating cumulus towers. *Monthly Weather Review*, *97*(7), 471–489. https://doi.org/10.1175/1520-0493(1969)097<0471:mopct>2.3.co;2

Stephens, G. L., L'Ecuyer, T., Forbes, R., Gettelmen, A., Golaz, J. C., Bodas-Salcedo, A., et al. (2010). Dreary state of precipitation in global models. *Journal of Geophysical Research*, *115*(D24). https://doi.org/10.1029/2010jd014532

Stephens, G. L., Vane, D. G., Tanelli, S., Im, E., Durden, S., Rokey, M., et al. (2008). CloudSat mission: Performance and early science after the first year of operation. *Journal of Geophysical Research*, *113*(D8). https://doi.org/10.1029/2008jd009982

Stevens, B., Satoh, M., Auger, L., Biercamp, J., Bretherton, C. S., Chen, X., et al. (2019). DYAMOND: The DYnamics of the atmospheric general circulation modeled on Non-hydrostatic domains [Dataset]. *Progress in Earth and Planetary Science*, *6*(1), 1–17. https://doi.org/10.1186/s40645-019-0304-z

Suzuki, K., Stephens, G., Bodas-Salcedo, A., Wang, M., Golaz, J.-C., Yokohata, T., & Koshiro, T. (2015). Evaluation of the warm rain formation process in global models with satellite observations. *Journal of the Atmospheric Sciences*, *72*(10), 3996–4014. https://doi.org/10.1175/jas-d-14-0265.1

Takahashi, H., & Luo, Z. (2012). Where is the level of neutral buoyancy for deep convection? *Geophysical Research Letters*, *39*(15). https://doi.org/10.1029/2012GL052638

Takahashi, H., & Luo, Z. J. (2014). Characterizing tropical overshooting deep convection from joint analysis of CloudSat and geostationary satellite observations. *Journal of Geophysical Research: Atmospheres*, *119*(1), 112–121. https://doi.org/10.1002/2013JD020972

Takahashi, H., Luo, Z. J., Masunaga, H., Storer, R., & Noda, A. T. (2024). Investigating convective processes underlying ENSO: New insights into the fixed anvil temperature hypothesis. *Geophysical Research Letters*, *51*(6), e2023GL107113. https://doi.org/10.1029/2023GL107113

Takahashi, H., Luo, Z. J., & Stephens, G. (2021). Revisiting the entrainment relationship of convective plumes: A perspective from global observations. *Geophysical Research Letters*, *48*(6), e2020GL092349. https://doi.org/10.1029/2020GL092349

Takahashi, H., Luo, Z. J., Stephens, G., & Mulholland, J. P. (2023). Revisiting the land-ocean contrasts in deep convective cloud intensity using global satellite observations. *Geophysical Research Letters*, *50*(5), e2022GL102089. https://doi.org/10.1029/2022GL102089

Takahashi, H., Luo, Z. J., & Stephens, G. L. (2017). Level of neutral buoyancy, deep convective outflow, and convective core: New perspectives based on 5 years of CloudSat data. *Journal of Geophysical Research: Atmospheres*, *122*(5), 2958–2969. https://doi.org/10.1002/2016JD025969

van den Heever, S. C. (2021). NASA selects new mission to study storms, impacts on climate models. *NASA Earth*. Retrieved from https://www.nasa.gov/press-release/nasa-selects-new-mission-to-study-storms-impacts-on-climate-models

Wang, D., Giangrande, S. E., Bartholomew, M. J., Hardin, J., Feng, Z., Thalman, R., & Machado, L. A. (2018). The green ocean: Precipitation insights from the GoAmazon2014/5 experiment. *Atmospheric Chemistry and Physics*, *18*(12), 9121–9145. https://doi.org/10.5194/acp-18-9121-2018

Wehr, T., Kubota, T., Tzeremes, G., Wallace, K., Nakatsuka, H., Ohno, Y., et al. (2023). The EarthCARE mission–science and system overview. *Atmospheric Measurement Techniques*, *16*(15), 3581–3608. https://doi.org/10.5194/amt-16-3581-2023

Williams, E., & Stanfill, S. (2002). The physical origin of the land–ocean contrast in lightning activity. *Comptes Rendus Physique*, *3*(10), 1277–1292. https://doi.org/10.1016/s1631-0705(02)01407-x

Yuter, S. E., & Houze Jr, R. A. (1995). Three-dimensional kinematic and microphysical evolution of Florida cumulonimbus. Part II: Frequency distributions of vertical velocity, reflectivity, and differential reflectivity. *Monthly Weather Review*, *123*(7), 1941–1963. https://doi.org/10.1175/1520-0493(1995)123<1941:tdkame>2.0.co;2

Zipser, E. J., Cecil, D. J., Liu, C., Nesbitt, S. W., & Yorty, D. P. (2006). Where are the most intense thunderstorms on Earth? *Bulletin of the American Meteorological Society*, *87*(8), 1057–1072. https://doi.org/10.1175/bams-87-8-1057